

Spatial and Kinematic Alignments between Central and Satellite Halos

A. FALTENBACHER,¹ Y. P. JING,¹ CHENG LI,¹ SHUDE MAO,² H. J. MO,³ ANNA PASQUALI,⁴ AND FRANK C. VAN DEN BOSCH⁴

Received 2007 June 2; accepted 2007 October 10

ABSTRACT

Based on a cosmological N -body simulation, we analyze spatial and kinematic alignments of satellite halos within 6 times the virial radius of group-sized host halos (r_{vir}). We measure three different types of spatial alignment: halo alignment between the orientation of the group central substructure (GCS) and the distribution of its satellites, radial alignment between the orientation of a satellite and the direction toward its GCS, and direct alignment between the orientation of the GCS and that of its satellites. Analogously, we use the directions of satellite velocities and probe three further types of alignment: the radial velocity alignment between the satellite velocity and the connecting line between the satellite and GCS, the halo velocity alignment between the orientation of the GCS and satellite velocities, and the autovelocity alignment between the satellite orientations and their velocities. We find that satellites are preferentially located along the major axis of the GCS within at least $6r_{\text{vir}}$ (the range probed here). Furthermore, satellites preferentially point toward the GCS. The most pronounced signal is detected on small scales, but a detectable signal extends out to $\sim 6r_{\text{vir}}$. The direct alignment signal is weaker; however, a systematic trend is visible at distances $\lesssim 2r_{\text{vir}}$. All velocity alignments are highly significant on small scales. The halo velocity alignment is constant within $2r_{\text{vir}}$ and declines rapidly beyond. The halo and the autovelocity alignments are maximal at small scales and disappear beyond $1r_{\text{vir}}$ and $1.5r_{\text{vir}}$, respectively. Our results suggest that the halo alignment reflects the filamentary large-scale structure that extends far beyond the virial radii of the groups. In contrast, the main contribution to the radial alignment arises from the adjustment of the satellite orientations in the group tidal field. The projected data reveal good agreement with recent results derived from large galaxy surveys.

Subject headings: dark matter — galaxies: clusters: general — galaxies: kinematics and dynamics — methods: numerical

1. INTRODUCTION

Over the last decades, observational and numerical evidence has substantiated the picture of a filamentary large-scale structure in the universe. In principle, the large-scale tidal field is expected to induce large-scale correlations between the orientations of halos and galaxies that are embedded within these filaments (e.g., Pen et al. 2000; Croft & Metzler 2000; Heavens et al. 2000; Catelan et al. 2001; Crittenden et al. 2001; Porciani et al. 2002; Jing 2002). On the other hand, the subsequent accretion onto larger systems, such as groups and clusters of galaxies, may alter the orientations of these (sub)structures in response to the local tidal field (Ciotti & Dutta 1994; Lee et al. 2005). Cosmological N -body simulations provide a valuable tool to differentiate the various contributions to the halo/galaxy alignments within overdense regions.

Observationally, various types of alignment between galaxies and their environment have been detected on a wide range of scales, from supercluster systems down to the distribution of the satellite galaxies in our Milky Way (MW). On cluster scales, various types of alignment are discussed in the literature: alignment between neighboring clusters (Binggeli 1982; Ulmer et al. 1989; West 1989; Plionis 1994; Chambers et al. 2002), between brightest cluster galaxies (BCGs) and their parent clusters (Carter & Metcalfe 1980; Binggeli 1982; Struble 1990; Rhee & Latour

1991; Plionis & Basilakos 2002), between the orientation of satellite galaxies and the orientation of the cluster (Dekel 1985; Plionis et al. 2003), and between the orientation of satellite galaxies and the orientation of the BCG (Struble 1990). According to these studies, the typical scales over which clusters reveal signs for alignment range up to $10\text{--}50 h^{-1}$ Mpc, which can be most naturally explained by the presence of filaments.

With large galaxy redshift surveys, such as the Two-Degree Field Galaxy Redshift Survey (2dFGRS; Colless et al. 2001) and the Sloan Digital Sky Survey (SDSS; York et al. 2000), it has recently also become possible to investigate alignments on group scales using large homogeneous samples. This has resulted in robust detections of various alignments: Brainerd (2005), Yang et al. (2006), and Azzaro et al. (2007) all found that satellite galaxies are preferentially distributed along the major axes of their host galaxies, while Pereira & Kuhn (2005) and Agustsson & Brainerd (2006a) noted that satellite galaxies tend to be oriented toward the galaxy at the center of the halo.

In contradiction to the studies above, Holmberg (1969) found that satellites around isolated late-type galaxies preferentially lie along the minor axis of the disk. Subsequent studies, however, were unable to confirm this so-called Holmberg effect (Hawley & Peebles 1975; Sharp et al. 1979; MacGillivray et al. 1982; Zaritsky et al. 1997). Recently, Agustsson & Brainerd (2007) reported a Holmberg effect at large projected distances around blue host galaxies, while on smaller scales the satellites were found to be aligned with the major axis of their host galaxy, and Bailin et al. (2007) claim that a careful selection of isolated late-type galaxies reveals the tendency of the satellites to align with the minor axis of the galactic disk. Investigating the companions of M31, Koch & Grebel (2006) find little evidence for a Holmberg effect. Yet, the Milky Way (MW) seems to exhibit a Holmberg effect even on small scales, in that the 11 innermost MW satellites

¹ Shanghai Astronomical Observatory, Joint Center for Cosmology and Astrophysics of the Max-Planck-Institut für Astrophysik and the Shanghai Astronomical Observatory, Nandan Road 80, Shanghai 200030, China.

² University of Manchester, Jodrell Bank Observatory, Macclesfield, Cheshire SK11 9DL, UK.

³ Department of Astronomy, University of Massachusetts, Amherst MA 01003-9305.

⁴ Max-Planck-Institute for Astronomy, Königstuhl 17, D-69117 Heidelberg, Germany.

show a pronounced planar distribution oriented nearly perpendicular to the MW disk (Lynden-Bell 1982; Majewski 1994; Kroupa et al. 2005; Kang et al. 2005; Libeskind et al. 2005).

Numerical simulations have been employed to test alignment on a similar range in scales, from superclusters down to galaxy-satellite systems. All studies focusing on cluster-sized halos report a correlation in the orientations for distances of at least $10 h^{-1}$ Mpc; some studies observe a positive alignment signal up to $100 h^{-1}$ Mpc (e.g., Onuora & Thomas 2000; Faltenbacher et al. 2002, 2005; Hopkins et al. 2005; Kasun & Evrard 2005; Basilakos et al. 2006). These findings are interpreted as the signature of the filamentary network that interconnects the clusters. The preferential accretion along these filaments causes the clusters to point toward each other. Also, for galaxy- and group-sized halos a tendency to point toward neighboring halos is detected. According to Altay et al. (2006), the alignments for such intermediate-mass objects are caused by tidal fields rather than accretion along the filaments. Consequently, the mechanisms responsible for the alignment of the orientations depend on halo mass. Further evidence for a mass dependence of alignment effects comes from the examination of the halos' angular momenta. Bailin & Steinmetz (2005) and Aragón-Calvo et al. (2007) find that the spins of galaxy-sized halos tend to be parallel to the filaments, whereas the spins of group-sized halos tend to be perpendicular. This behavior may originate in the relative sizes of halos with respect to the surrounding filaments.

On subhalo scales, basically three different types of alignments have been discussed: the alignment of the overall subhalo distribution with the orientation of the host halo (e.g., Knebe et al. 2004; Zentner et al. 2005; Agustsson & Brainerd 2006b; Kang et al. 2007; Libeskind et al. 2007), the alignment of the orientations of subhalos among each other (e.g., Lee et al. 2005), and, very recently, the orientation of the satellites with respect to the center of the host (Kuhlen et al. 2007; Pereira et al. 2008). Again, accretion along the filaments and the impact of tidal fields have been invoked to explain the former and the latter, respectively. Thus, on all scales, tidal fields and accretion along filaments are considered to be the main contributors to the observed alignment signals. Here we attempt to isolate the different contributions. In particular, we focus on the continuous transition from subhalo to halo scales, meaning that we examine the alignment of (sub)structure on distance scales between 0.3 and 6 times the virial radius of group-sized halos.

Faltenbacher et al. (2007, hereafter Paper I) applied the halo-based group finder of Yang et al. (2005) to the SDSS Data Release 4 (DR4; Adelman-McCarthy et al. 2006) and carried out a study of the mutual alignments between central galaxies (BCGs) and their satellites in group-sized halos. Using the same data set, consisting of over 60,000 galaxies, three different types of alignment have been investigated: (1) the halo alignment, between the orientation of the BCG and the associated satellite distribution; (2) the radial alignment, between the direction given by the BCG-satellite connection line and the satellite orientation; and (3) the direct alignment, between the orientation of the BCG and the satellite. The study presented in this paper focuses on the same types of alignment and is aimed to compare the observational results with theoretical expectations derived from N -body simulations.

There are a variety of dynamical processes that can contribute to the alignments of satellites associated with groups. The most important are (1) a possible preadjustment of satellites in the filaments, which for distances of a few times the virial radius commonly points radially toward the group; (2) the preferential accretion along those filaments; (3) the change of the satellite

orbits in the triaxial group potential well; and (4) the continuous readjustment of satellite orientations as they orbit within the group. Basically, the first two points can be attributed to the large-scale environment of the groups, whereas the latter two are more closely associated with the impact of the group potential on small scales. The purpose of the present analysis is to separate the different contributions to the observed alignment signals; therefore we analyze the mutual orientations of satellites within 6 times the virial radius of the groups. Since the tidal forces are closely related to the dynamics of the satellites, additional insight into the generation of alignment can be gained by considering the satellite velocities. Therefore, we also investigate the direction of the satellite velocities with respect to their orientations, which constitutes an indirect way to infer the impact of the dynamics on the orientation of the satellites. A more direct way to work out the interplay between the dynamics and the orientations would be to trace the orbits of individual satellites; however, such an approach goes beyond the scope of the present study.

The paper is organized as follows. In § 2 we introduce the simulation and describe the halo-finding procedure. Section 3 deals with some technical aspects, namely, the determination of the size and orientation of the substructures. In § 4 we present the signals of the three-dimensional spatial and velocity alignments, and in § 5 we repeat the analysis based on projected data. Finally, we conclude with a summary in § 6.

2. SIMULATION AND HALO IDENTIFICATION

For the present analysis we employ an N -body simulation of structure formation in a flat Λ CDM universe with a matter density $\Omega_m = 0.3$, a Hubble parameter $h = H_0/(100 \text{ km s}^{-1} \text{ Mpc}^{-1}) = 0.7$, and a Harrison-Zeldovich initial power spectrum with normalization $\sigma_8 = 0.9$. The density field is sampled by 512^3 particles within a $100 h^{-1}$ Mpc cube, resulting in a mass resolution of $6.2 \times 10^8 h^{-1} M_\odot$. The softening length was set to $\epsilon = 10 h^{-1} \text{ kpc}$, beyond which the gravitational force between two particles is exactly Newtonian. The density field is evolved with 5000 time steps from an initial redshift of $z_i = 72$ using a particle-particle-particle-mesh (P^3M) solver. An extensive description of the simulation can be found in Jing & Suto (2002), where it is called LCDMa realization.

As detailed in the following two paragraphs, the host halos and their satellites are found in two subsequent steps with two different techniques; first the main halos are located, and thereafter the associated satellite halos are searched for. In order to identify the host halos, we first run a friends-of-friends (FoF) algorithm (Davis et al. 1985) on the simulation output at $z = 0$. We set the FoF linking length to 0.1 times the mean particle separation, which selects regions with an average overdensity of ~ 3000 . Note that this linking length is a factor of 2 smaller than the commonly used value of 0.2; consequently, only the central part of the host halo (and occasionally large substructures) is selected. Subsequently, the virial radius, r_{vir} , is defined as the radius of the sphere centered on the most bound FoF particle, which includes a mean density of 101 times the critical density, and we simply define the virial mass of each halo as the mass within r_{vir} . If the virial regions of two halos overlap, the lower mass halo is discarded. In what follows, we focus only on the 515 halos with a virial mass in the range from 10^{13} to $5 \times 10^{14} h^{-1} M_\odot$ (corresponding to halos with more than 16,000 particles). Since this is the typical mass scale of galaxy groups, we refer to these halos as "groups."

In a second step, we search for self-bound (sub)structures using the SKID halo finder (Stadel 2001) applied to the particle distribution within groupcentric distances of $6r_{\text{vir}}$. As discussed in

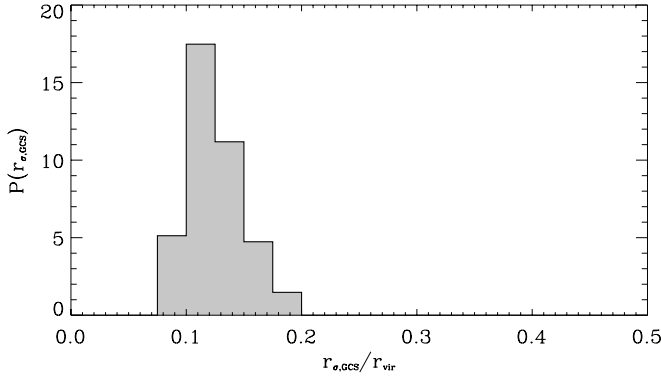


FIG. 1.—Distribution of the spatial dispersion r_σ of the group central substructure (GCS) in units of the virial radius. Satellites can be resolved only at radii larger than the size of the GCS.

Macciò et al. (2006), SKID adequately identifies the smallest resolvable substructures when using a linking length l equal to twice the softening length, i.e., 4 times the spline-softening length. We therefore adopt $l = 20 h^{-1}$ kpc. Throughout, we distinguish between group central substructures (GCSs), which are located at the center of our groups, and satellites, which are all the other (sub)structures, no matter whether they lie within or beyond r_{vir} . According to this definition, every group hosts one, and only one, GCS at its center, while it may have numerous satellites outside the volume occupied by the GCS. Satellites are assigned to all groups from which they are separated by less than $6r_{\text{vir}}$. Hence, a satellite may be assigned to more than one GCS.

3. SIZE AND ORIENTATION OF SUBSTRUCTURES

Before describing the computation of the orientation, we determine the typical sizes of the GCSs and the satellites. Knowledge about the physical sizes of the (sub)structures provides a crucial link for making the comparison to observational data.

3.1. Sizes of Group Central Substructures

The physical interpretation of the size of the GCS is not straightforward. For one thing, it depends on the SKID linking length used. However, for our purposes it is sufficient to note that the GCS represents the dense inner region of the group, which, largely for numerical reasons, is free of substructure. Consequently, any radial dependence of satellite properties can be probed only down to the size of the GCS. In order to express the sizes of the GCS and the satellites, we use the rms of the distances between the bound particles, r_σ . The advantage of this size measure is that it provides a direct estimate of the (momentary) size without having to make any assumption regarding the actual density distribution. In the case of an isolated Navarro-Frenck-White (NFW) halo, $r_\sigma \approx 0.5r_{\text{vir}}$, with only a very weak dependence on the concentration parameter. Figure 1 displays the r_σ distribution of the GCSs in units of the group's virial radius, r_{vir} . The distribution peaks at $0.11r_{\text{vir}}$ and has a mean of $0.13r_{\text{vir}}$.

3.2. Sizes of Satellite Halos

The aim of the present analysis is twofold: (1) to assess the impact of the group tidal field on the satellite orientations and (2) to compare the alignment signals in our N -body simulation to observations of galaxy alignments. The impact of the group tidal field is stronger at larger satellitecentric radii. On the other hand, since galaxies reside at the centers of their dark matter halos, the central parts of the satellites are of more interest when comparing the alignment signals with those observed for galaxies.

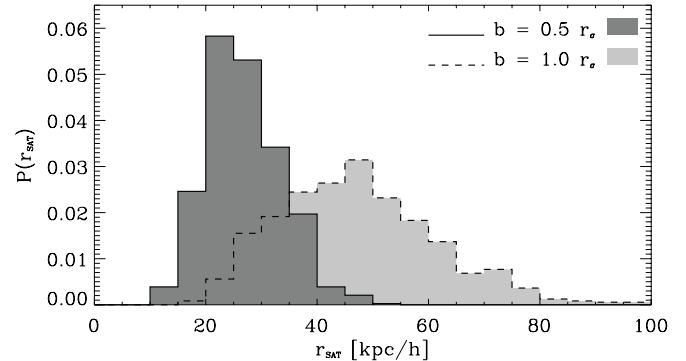


FIG. 2.—Distribution of the radii of satellites found within the virial radius of the group. In this context, “radius” refers to the listed fraction (0.5 and 1.0) of the satellites’ spatial dispersion r_σ . For example, the typical inner radii probed by the $b = 0.5r_\sigma$ sample is $\sim 30 h^{-1}$ kpc.

To meet both requirements, we therefore measure the orientation of the satellite mass distribution within two radii. Analogous to the measurement of GCS sizes, we determine these radii with reference to the spatial dispersion r_σ . More precisely, we choose the particles within $1.0r_\sigma$ and $0.5r_\sigma$ as the basic sets to determine the satellite orientation (see § 3.3). Figure 2 displays the distributions of the corresponding physical sizes. The $0.5r_\sigma$ sample probes the matter distribution of the satellites within $\sim 25 h^{-1}$ kpc, which is comparable to the sizes of elliptical galaxies. The mean physical radii of the $1.0r_\sigma$ sample is $\sim 50 h^{-1}$ kpc. If not stated otherwise, we display the results for the $0.5r_\sigma$ sample, since this may most closely resemble the properties of observable galaxy distributions (outside of the very central part of the host halo).

3.3. Orientation

There are a few different ways found in the literature (e.g., Bullock 2002; Jing & Suto 2002; Bailin & Steinmetz 2005; Kasun & Evrard 2005; Allgood et al. 2006) to model halos as ellipsoids. They all differ in details, but most methods model halos using the eigenvectors from some form of the inertia tensor. The eigenvectors correspond to the direction of the major axes, and the eigenvalues to the lengths of the semimajor axes $a \geq b \geq c$. Following Allgood et al. (2006), we determine the main axes by iteratively computing the eigenvectors of the *distance-weighted* inertia tensor,

$$I_{ij} = \sum_{k=1,N} \frac{r_{ki}r_{kj}}{r_k^2}, \quad (1)$$

where r_{ki} denotes the i th component of the position vector of the k th particle with respect to the center of mass and

$$r_k = \sqrt{\frac{x^2}{a^2} + \frac{y^2}{b^2} + \frac{z^2}{c^2}} \quad (2)$$

is the elliptical distance in the eigenvector coordinate system from the center to the k th particle. The square roots of the eigenvalues of the inertia tensor determine the axial ratios of the halo ($a:b:c = \sqrt{\lambda_a}:\sqrt{\lambda_b}:\sqrt{\lambda_c}$). The iteration is initialized by computing the eigenvalues of the inertia tensor for the spherically truncated halo. In the following iterations, the length of the intermediate axis is kept unchanged, and all bound particles within the ellipsoidal window determined by the eigenvalues of the foregoing iteration are used to compute the new inertia tensor. The iteration is completed when the eigenvectors have converged. The direction of the resulting major axis is identified

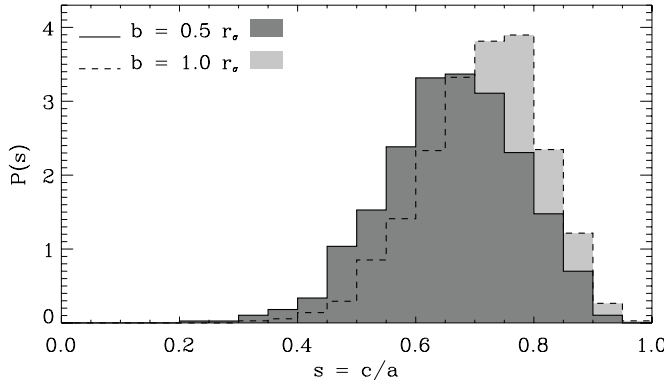


FIG. 3.—Distribution of satellite shapes, represented by the ratio of the shortest to the longest semimajor axis of the mass ellipsoid ($s = c/a$). The colors correspond to the samples with different truncation radii as listed. With increasing size, the halos become rounder. The distribution of the $b = 0.5r_\sigma$ sample is rather symmetric, whereas for larger truncation radii there appears a slight asymmetry.

as the orientation. The advantage of keeping the intermediate axis fixed is that the number of particles within the varying ellipsoidal windows remains almost constant. Instead, if the longest (shortest) axis is kept constant, the number of particles within the ellipsoidal windows can decrease (increase) substantially during the iteration.

Note that we apply this truncation to all (sub)structures, both satellites and GCSs, and that the orientation of each sub(structure) is measured within this truncation radius. Throughout, we consider only those sub(structures) that comprise at least 200 bound particles within the volume of the final ellipsoid (corresponding to a lower limit in mass of $\approx 10^{11} h^{-1} M_\odot$). For the satellites this implies that a smaller truncation radius results in a smaller sample. For example, there are 772 $0.5r_\sigma$ satellites within the virial radii of our groups, whereas the $1.0r_\sigma$ sample comprises 1431 satellites. Since all 515 GCSs contain more than 200 particles within $0.5r_\sigma$, their sample size is independent of the truncation radius used.

Figure 3 displays the distribution of the shape parameter $s = c/a$. The shading corresponds to different truncation radii as listed. There is a weak indication that satellites become more spherical with increasing truncation radii. A similar behavior was found for isolated halos (e.g., Jing & Suto 2002; Allgood et al. 2006). As discussed by Allgood et al. (2006), the exact determination of individual shapes may need as many as 7000 particles, so that the resolution of the present simulation is not suited for the analysis of (sub)structure shapes. However, for the determination of the orientations, which is the focus of this paper, a particle limit of 200 can be considered conservative (cf. Jing 2002; Pereira et al. 2008). A study examining the shapes of substructure in a single high-resolution Milky Way-sized halo can be found in Kuhlen et al. (2007).

4. THREE-DIMENSIONAL ALIGNMENTS

For both classes of objects, GCSs and satellites, the orientations are determined according to the approach described above. A third orientation-like quantity is given by the direction of the line connecting a GCS-satellite pair. Throughout, we refer to the orientation of the GCS, the satellite, and the connecting line as \mathbf{a}_{GCS} , \mathbf{a}_{SAT} , and \mathbf{r} , respectively. These quantities are unit vectors, such that the scalar product of two vectors yields the cosine of the angle between them. We focus on three different types of alignment, (1) the halo alignment between the orientations of the GCSs and the connecting lines, (2) the radial alignment between the orientations of the satellites and the connecting lines, and (3) the

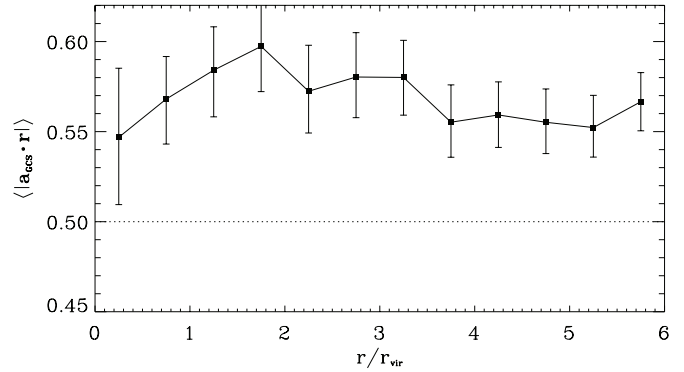


FIG. 4.—Mean values of the cosines of the angles between the orientations of the GCSs and the connecting lines to the satellites, $\langle |\mathbf{a}_{\text{GCS}} \cdot \mathbf{r}| \rangle$, as a function of r/r_{vir} for the $0.5r_\sigma$ sample. The dotted horizontal line indicates the mean values for an isotropic distribution. The error bars indicate the 95% bootstrap confidence intervals within each distance bin.

direct alignment between the orientation of the GCS and that of its satellites. We also consider various alignments based on the proper velocity, \mathbf{v} , of the satellite with respect to its GCS. In particular, we discuss (4) the radial velocity alignment between \mathbf{v} and \mathbf{r} , (5) the halo velocity alignment between \mathbf{a}_{GCS} and \mathbf{v} , and finally (6) the autovelocities alignment between the orientations, \mathbf{a}_{SAT} , and velocities, \mathbf{v} , of the satellites. Here \mathbf{v} is the unit vector indicating the direction of the *proper* velocity of the satellite (including the Hubble flow) relative to the host. Since all the other quantities also represent unit vectors, the scalar products yield the cosines of the enclosed angles.

4.1. Halo Alignment

In order to measure the alignment between the GCS and the satellite distribution, we use \mathbf{a}_{GCS} and \mathbf{r} (the orientation of the GCS and the position of the satellite with respect to its GCS). Figure 4 displays the radial dependence of $\langle |\mathbf{a}_{\text{GCS}} \cdot \mathbf{r}| \rangle$ within $6r_{\text{vir}}$, where angle brackets denote the mean value within a bin of r/r_{vir} . The error bars indicate the 95% bootstrap confidence intervals based on 1000 bootstrap samples for each distance bin.

Over the entire range of distances probed, the mean values of the cosines deviate significantly from an isotropic distribution. The strength of the alignment, i.e., the deviation from $\langle |\mathbf{a}_{\text{GCS}} \cdot \mathbf{r}| \rangle = 0.5$, increases with groupcentric distance and reaches a maximum at $\sim 1.7r_{\text{vir}}$. The subsequent decline, however, is very weak, and even at $6r_{\text{vir}}$ the alignment is still very pronounced ($\langle |\mathbf{a}_{\text{GCS}} \cdot \mathbf{r}| \rangle \approx 0.55$), with no clear indication of a downward trend. The fact that there is strong alignment over such a long range suggests that the intrinsic halo alignment is closely connected to the filamentary structure in which the groups are embedded. Since here we focus on the transition between group- and environment-dominated areas, we do not aim to map out the entire range of the radial alignment.

The weakening of the signal at small scales may be attributed to the fact that the information about the filamentary origin is washed away once the satellites start to orbit within the groups (i.e., once nonlinear effects kick in). Yet, the orientation of the group itself is closely correlated with the surrounding filamentary network, so that a residual alignment is maintained by the overall distribution of satellites orbiting in the potential well of the group (cf. Statler 1987; Zentner et al. 2005; Kang et al. 2007). In addition, if one assumes that filaments are approximately cylindrical and that the GCS is aligned with the orientation of the cylinder, then the mean angles between the orientation of the GCS and the satellites position become larger at smaller groupcentric radii. In fact, at distances smaller than the radius of the cylinder, the

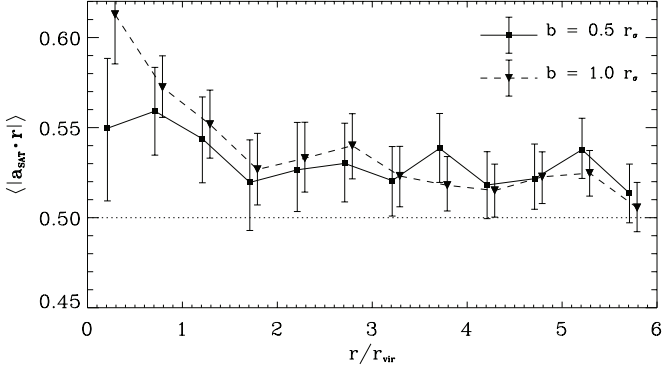


FIG. 5.—Same as Fig. 4, but for the mean values of cosines between the satellite orientation and the connecting line to the GCS, $\langle |a_{\text{SAT}} \cdot r| \rangle$ for the $0.5r_\sigma$ and $1.0r_\sigma$ samples.

distribution will converge to isotropic. Finally, some contribution to the decrease of the alignment strength on small scales may come from the fact that satellites on nearly radial orbits are filtered out during their epicenter passage. They get severely stripped, and consequently, the number of particles that remains bound can easily fall below the detection criterion (minimum of 200 particles), thus weakening the alignment signal.

4.2. Radial Alignment

The radial alignment, $\langle |a_{\text{SAT}} \cdot r| \rangle$, probes the orientations of individual satellites, a_{SAT} , relative to the direction pointing toward their GCS, r . Figure 5 displays $\langle |a_{\text{SAT}} \cdot r| \rangle$ for distances up to $6r_{\text{vir}}$. The line styles represent different truncation radii of the satellites. Over the entire range of groupcentric distances probed, the data reveal a significant anisotropic distribution. The signal is most pronounced on small scales, where it also shows a strong dependence on the truncation radii. The $1.0r_\sigma$ sample, which includes the behavior of the outer mass shells of the satellites, clearly exhibits a stronger deviation from isotropy. Within $\sim 1.5r_{\text{vir}}$ there is a pronounced decline of the radial alignment signal, while it remains remarkably constant at larger radii. For distances in the range between $2r_{\text{vir}}$ and $6r_{\text{vir}}$ we detect a weak but significant signal, $\langle |a_{\text{GCS}} \cdot a_{\text{SAT}}| \rangle \approx 0.52$, inconsistent with isotropy at 95% confidence level, in good agreement with Hahn et al. (2007). In a recent study, Kuhlen et al. (2007) detected no radial alignment for distances $\gtrsim 3r_{\text{vir}}$. However, their analysis is based on a re-simulation of a single galaxy-sized host halo. Since this halo is rather isolated, in that it has not experienced any major merger since redshift $z = 1.7$, it is likely that its ambient filaments have already been drained.

At large distances, satellites preferentially reside in filaments (as discussed in the context of Fig. 4), which point radially toward the groups. Consequently, the signal on scales $\gtrsim 2r_{\text{vir}}$ indicates an alignment between the satellite orientations and the filaments in which they are embedded. Such an alignment may be caused by accretion of matter along those filaments or by the local tidal fields generated by the mass distribution within the filaments. The group tidal field is not likely to be responsible for the observed large-scale alignment signal due to its rapid decline with distance. On small scales, however, the tidal field can substantially alter the orientations of the satellites. As shown by Ciotti & Dutta (1994), the timescale on which a prolate satellite can adjust its orientation to the tidal field of a group is much shorter than the Hubble time, but longer than its intrinsic dynamical time. Therefore, the adjustment of the satellite orientations parallel to the

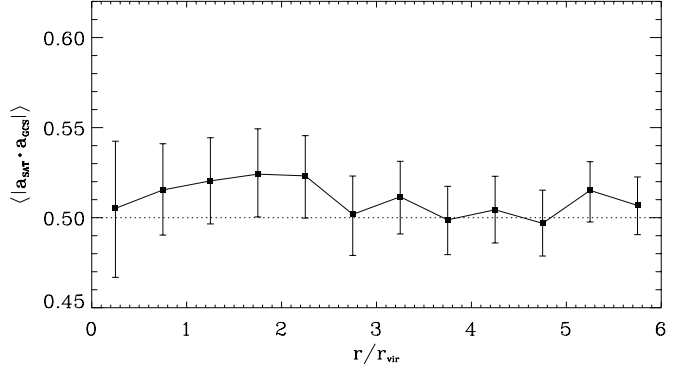


FIG. 6.—Same as Fig. 4, but for the mean values of cosines between the orientation of the satellites and the GCS, $\langle |a_{\text{SAT}} \cdot a_{\text{GCS}}| \rangle$.

gradients of the group potential offers a convincing explanation for a radial alignment signal on small scales. This perception is further supported by the dependence of the alignment strength on the truncation radii of the satellites. For the largest radii, which are most strongly affected by tidal forces, the alignment signal is strongest.

4.3. Direct Alignment

The strong signals for halo and radial alignment may lead to the expectation of a comparably pronounced signal for the direct alignment between the orientation of the GCS, a_{GCS} , and the orientations of its satellites, a_{SAT} . However, as can be seen in Figure 6, the signal is weak. There is only a weak trend for positive alignment up to $2r_{\text{vir}}$. The significance found at distances between $1r_{\text{vir}}$ and $\sim 2r_{\text{vir}}$ seems to be somewhat higher ($\sim 90\%$ confidence). Based on an analytical model, Lee et al. (2005) predict a certain degree of parallel alignment between host and satellite orientations due to the evolution of the satellites within the tidal shear field of the host. The signal for the direct alignment may be a relic of this effect.

To summarize, we find positive alignment signals for all three types of alignment tested here. However, they differ in strength and radial extent. The halo alignment is the strongest and reaches far beyond the virial radii of the groups ($\gtrsim 6r_{\text{vir}}$). The radial alignment is most pronounced at small scales, where it reveals a strong dependence on the radial extent of the satellite over which its orientation has been measured. Although the radial alignment is weak beyond $\sim 1.5r_{\text{vir}}$, the signal stays remarkably constant out to $\sim 6r_{\text{vir}}$. Finally, the least prominent signal comes from the direct alignment. This ranking of the alignment strengths is in good agreement with the observational results reported in Paper I.

4.4. Alignments Based on Subhalo Velocities

If tidal forces give rise to the radial alignment on small scales, as displayed in Figure 5, the satellite orientations should be related to their actual velocities and the local gradients of the host potential. For instance, a satellite moving radially toward the GCS will show an enhanced radial alignment, since the gradient of the potential and the actual velocity are pointing in the same direction, inducing an orientation in the radial direction. On the other side, the orientations of satellites moving perpendicular to the gravitational field (i.e., tangentially with respect to the GCS) will lie between their velocities and the gradients of the potential well. To gain some more insight into the dynamical origin of the alignments, we include the directions of satellite velocities in the alignment

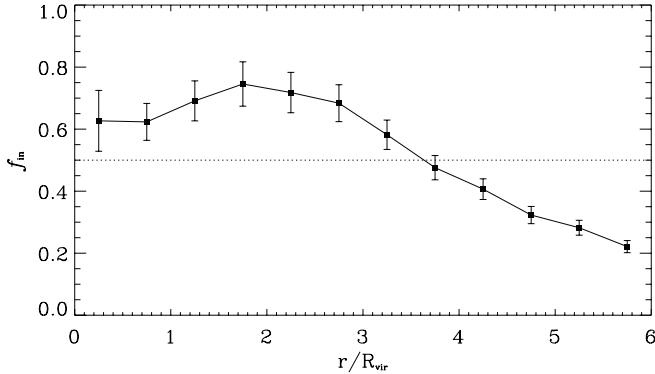


FIG. 7.—Ratio of inward-moving satellites, $f_{\text{in}} = n_{\text{in}} / (n_{\text{out}} + n_{\text{in}})$ for the $0.5r_{\sigma}$ sample. Error bars are Poisson.

study. We consider three different kinds of alignments, the radial velocity alignment, $|\mathbf{v} \cdot \mathbf{r}|$, the halo velocity alignment $|\mathbf{a}_{\text{GCS}} \cdot \mathbf{v}|$, and the autovelocities alignment $|\mathbf{a}_{\text{SAT}} \cdot \mathbf{v}|$.

To facilitate the interpretation of the velocity alignments, we split the satellites according to whether their net motion is inward ($\mathbf{v} \cdot \mathbf{r} < 0$) or outward ($\mathbf{v} \cdot \mathbf{r} > 0$) with respect to their group. Figure 7 shows the fraction of inward-moving satellites, f_{in} , as a function of their groupcentric distances. Note that f_{in} reaches a maximum around $\sim 2r_{\text{vir}}$, beyond which the Hubble flow gradually starts to become more and more important. In fact, at sufficiently large radii, where the Hubble flow dominates, one expects that $f_{\text{in}} = 0$, and all satellites reveal an outward motion. For satellites that are in virial equilibrium within the group potential (i.e., at $r \lesssim r_{\text{vir}}$), one expects roughly equal numbers of inward- and outward-moving systems (i.e., $f_{\text{in}} = 0.5$). However, on these small scales, one has an additional contribution from the infall region around the group, causing $f_{\text{in}} > 0.5$. In addition, a substantial fraction of satellites get stripped below the detection limit (200 particles) at their pericentric passage, so that they no longer contribute to the signal on their outward motion (cf. Faltenbacher & Mathews 2007). At r_{vir} , the outgoing satellite fraction is about 40%, which is (within the errors) consistent with the value $\sim 30\%$ determined by Wang et al. (2005). If one assumes an average ratio of 6 : 1 between apo- and pericenter distances for typical satellite orbits (Ghigna et al. 1998; van den Bosch et al. 1999), the majority of these satellites must have passed the central parts of the group before (cf. Kuhlen et al. 2007).

The top panel of Figure 8 displays the radial velocity alignment, $\langle |\mathbf{v} \cdot \mathbf{r}| \rangle$, as a function of r/r_{vir} . The condition $\langle |\mathbf{v} \cdot \mathbf{r}| \rangle > 0.5$ indicates that the distribution of angles between \mathbf{r} and \mathbf{v} is not isotropic; instead, on average they preferentially point in radial directions. This behavior is in agreement with earlier studies of the velocity anisotropy of subhalos, which is usually expressed by the anisotropy parameter $\beta = 1 - 0.5(\sigma_t/\sigma_r)^2$ (e.g., Binney & Tremaine 1987), where σ_t and σ_r denote the velocity dispersions of the satellites in the tangential and radial direction, respectively. Note that $\langle |\mathbf{v} \cdot \mathbf{r}| \rangle$ is closely related to β . If one assumes a relaxed (steady state) halo, the aforementioned tendency toward radial motions translates into a higher radial velocity dispersion compared to the tangential one, $\sigma_r > \sigma_{t1} = \sigma_t/\sqrt{2}$ (where σ_{t1} and σ_t are the one- and two-dimensional tangential velocity dispersions, respectively, and tangential isotropy is assumed). Thus $\langle |\mathbf{v} \cdot \mathbf{r}| \rangle > 0.5$ on small scales ($r \lesssim 2r_{\text{vir}}$) suggests that $\sigma_r > \sigma_t/\sqrt{2}$, in good qualitative agreement with numerical simulations that have shown that $\beta > 0$ for subhalos within the virial radius of their hosts (Ghigna et al. 1998; Colín et al. 2000; Diemand et al. 2004).

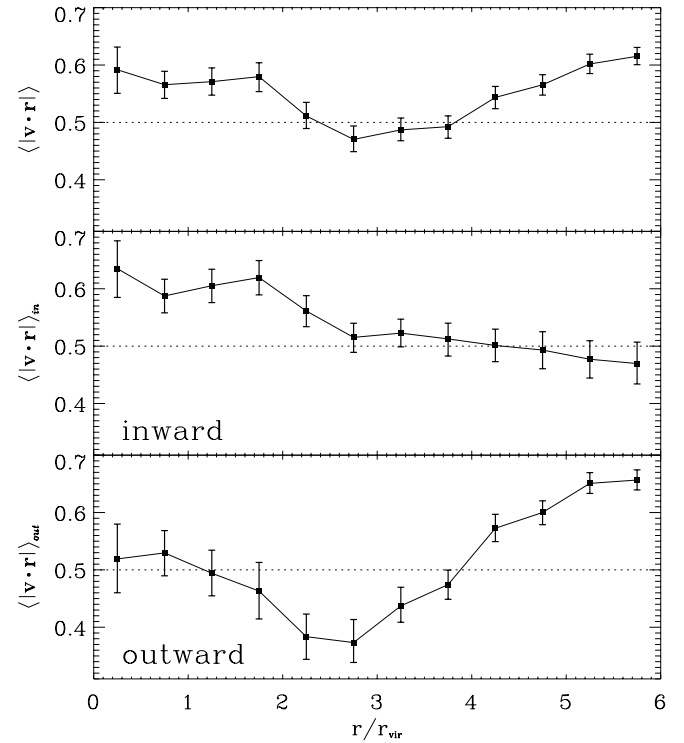
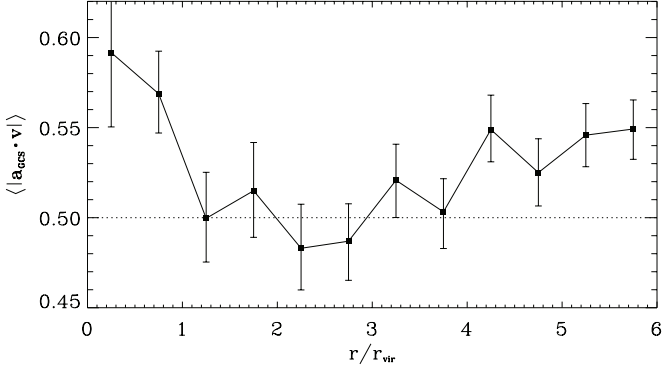


FIG. 8.—Same as Figure 4, but for $\langle |\mathbf{v} \cdot \mathbf{r}| \rangle$, displaying the signal for all satellites (top), the inward-moving satellites (middle), and the outward-moving satellites (bottom).

In accordance with the spherical collapse model, the signal extends out to $\sim 2r_{\text{vir}}$, which roughly reflects the distance of turnaround. At $2.5r_{\text{vir}}$ the distribution is close to isotropic, suggesting that at these distances the impact of the group potential is negligible, and the satellite motions are dominated by local potential variations arising from the filaments and dark matter halos within these filaments. Note that the presence of this filamentary structure in the vicinity of groups is clearly evident from Figure 4. Finally, the increase in the radial velocity alignment on large scales, $\gtrsim 4r_{\text{vir}}$, is simply due to the Hubble flow (i.e., $\langle |\mathbf{v} \cdot \mathbf{r}| \rangle \rightarrow 1$ at $r \rightarrow \infty$). The middle panel of Figure 8 shows $\langle |\mathbf{v} \cdot \mathbf{r}| \rangle$ for the inward-moving satellites only. The radial trend within $2r_{\text{vir}}$ is somewhat enhanced compared to the top panel. At larger radii, the inward-moving satellites have a velocity structure that is consistent with isotropy. The bottom panel of Figure 8 reveals a marked difference in the behavior of $\langle |\mathbf{v} \cdot \mathbf{r}| \rangle$ for the outward-moving satellites. It indicates a slightly radial trend for satellites within $1r_{\text{vir}}$, which is much lower than seen in the top two panels. Within $1r_{\text{vir}}$ or $2r_{\text{vir}}$ it drops below 0.5, indicating a preference for tangential velocities. Together with the information derived from Figure 7, this suggests that a substantial fraction of outward-moving satellites located at $1r_{\text{vir}}$ or $2r_{\text{vir}}$ currently are close to their apocenter passage after having crossed the more central regions of the group. Finally, on large scales, the outward-moving satellites clearly reveal the Hubble flow.

Figure 9 displays the radial dependence of $\langle |\mathbf{a}_{\text{GCS}} \cdot \mathbf{v}| \rangle$, which measures the cosines of the angles between the satellite velocities and the orientation of the GCS. On large scales, the radial outward motion caused by the Hubble flow exceeds the internal velocities of the satellites within the filaments. Since the GCS is strongly aligned with these filaments over the entire radial range shown (cf. Fig. 4), one has that $\langle |\mathbf{a}_{\text{GCS}} \cdot \mathbf{v}| \rangle > 0.5$ on scales where the Hubble flow becomes important ($\gtrsim 4r_{\text{vir}}$). The strong alignment

FIG. 9.—Same as Fig. 4, but for $\langle |a_{\text{GCS}} \cdot v| \rangle$.

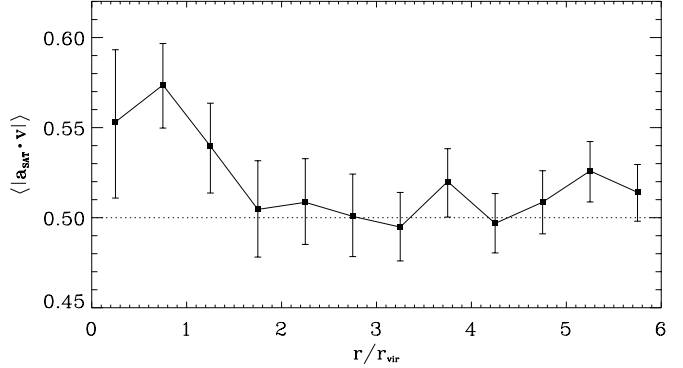
signal on small scales indicates that the satellites tend to move parallel to the orientation of the GCS. According to Tormen (1997) and Allgood et al. (2006), the principal axes of the velocity anisotropy tensor are strongly correlated with the principal axes of the satellite distribution. Therefore, the alignment found for $\langle |a_{\text{GCS}} \cdot v| \rangle$ (Fig. 4) actually implies an analogous signal for $\langle |a_{\text{GCS}} \cdot r| \rangle$. However, in contrast to the halo alignment, $\langle |a_{\text{GCS}} \cdot r| \rangle$, the velocity halo alignment, $\langle |a_{\text{GCS}} \cdot v| \rangle$, extends only out to $\sim 1r_{\text{vir}}$. Beyond this radius, a substantial fraction of the satellites show relatively large angles between their velocities and the orientation of the GCS, consistent with the picture of tangential motions associated with the apocenter passage of the satellites, as discussed in the context of Figure 8.

Finally we consider the autovelocity alignment, $\langle |a_{\text{SAT}} \cdot v| \rangle$, which reflects the distribution of the cosines between the satellite velocities and their orientations, $|v \cdot a_{\text{SAT}}|$. Figure 10 displays the variation of $\langle |a_{\text{SAT}} \cdot v| \rangle$ with r/r_{vir} .

The signal for $\langle |a_{\text{SAT}} \cdot v| \rangle$ shows a maximum at $0.7r_{\text{vir}}$. At larger distances, it decreases quickly. Beyond $1.5r_{\text{vir}}$, it is roughly in agreement with an isotropic distribution. One possible reason for the slight central dip is that satellites on their pericenter passages move perpendicular to the gradients of the group potential. Figure 5, however, revealed a preferential radial orientation of these satellites. Thus, during the pericenter passages, the angles between satellite orientations and velocities can become large. The degree of the radial alignment depends on the ratio between the internal dynamical time of the satellite, with which it can adjust its orientation, and the duration of the pericenter passage. If the pericenter passage occurs too quickly, the time may be too short for a “perfect” radial alignment (cf. Kuhlen et al. 2007). On large scales ($1r_{\text{vir}} - 2r_{\text{vir}}$) a similar mechanism may operate. We have argued above that within this distance range a substantial fraction of satellites are close to their apocenter passage. During this phase the velocities are again perpendicular to the gradient of the potential but, as indicated by Figure 5, the satellites are oriented radially. The comparison between the signal for $\langle |a_{\text{SAT}} \cdot r| \rangle$ and $\langle |a_{\text{SAT}} \cdot v| \rangle$ suggests that, in a statistical sense, the (spatial) radial alignment is maintained during the entire orbit of the satellite within the potential well of the groups, which in turn causes a suppression of $\langle |a_{\text{SAT}} \cdot v| \rangle$, at its apo- and pericenter.

5. PROJECTED ALIGNMENTS

To facilitate a comparison with observations, in particular with the results presented in Paper I, we repeat the foregoing analysis using projected data; i.e., we project the particle distribution along one of the coordinate axes and compute the second moment of mass for the projected particle distribution. Accordingly, for the distances between the GCS and its satellites, we use the projected

FIG. 10.—Same as Fig. 4, but for the mean values of cosines between the satellite velocities and positions, $\langle |v \cdot r| \rangle$.

values (all satellites within a sphere of $6r_{\text{vir}}$ about the GCS are projected), which we label R (the physical distances are labeled r).

Since the projections along the three Cartesian coordinate axes are independent, we include all three projections of each host-satellite in our two-dimensional sample. To reduce the contamination by satellites associated with massive ambient groups, we exclude those host-satellite systems where another SKID group more massive than the GCS (which is most likely the center of an ambient host-satellite system) is found within a sphere of $6r_{\text{vir}}$. After rejection of contaminated groups, we obtain, respectively, 1034 and 543 satellites for the $1.0r_{\sigma}$ and $0.5r_{\sigma}$ samples, with three-dimensional distances to the GCS $\leq r_{\text{vir}}$ (for all groups irrespective of their environment, we found 1431 and 772 satellites, respectively; see § 3.3.) Furthermore, since (for technical reasons) we project satellites located within a sphere of $6r_{\text{vir}}$, the projected volume at large projected distances shrinks substantially. Therefore, we analyze the two-dimensional data only for projected distances $\lesssim 3r_{\text{vir}}$, which roughly resembles the projection of all satellites within a cylinder of radius $3r_{\text{vir}}$ and length $10r_{\text{vir}}$ along the line of sight. Thus, in an approximate manner, uncertainties in the determination of group membership based on redshift measurements are accounted for.

The resolution of the simulation does not permit us to probe alignment below $0.3r_{\text{vir}}$. Other authors (using semianalytical techniques, e.g., Kang et al. 2007) have bypassed this problem by introducing so-called orphan galaxies, i.e., galaxies associated with the once most bound particle of a satellite halo, which subsequently has become undetectable due to stripping by tidal forces. Here we do not adopt this technique, since it does not provide us with information about the orientation of a satellite. Both approaches, considering only satellite halos with a minimum number of particles and the introduction of orphan galaxies, have certain disadvantages. The former does not account for galaxies that are hosted by strongly stripped subhalos, whereas the latter ignores the dynamical differences of galaxies and (once most bound) particles.

The application of a fixed lower particle limit excludes from the analysis satellites that still constitute distinct objects. In particular, satellites that are strongly tidally stripped may fall below the selection criterion even if the galaxy, which is assumed to lie at the center, is still observable. Thus, we caution that our satellite sample may be somewhat biased toward more recently accreted satellites compared to a hypothetical galaxy population. This effect appears whenever a fixed lower particle limit is imposed.

Analogous to Paper I, we define the angles θ , ϕ , and ξ to address the projected halo, radial, and direct alignments (same definitions as in § 4, but for the two-dimensional data; see Fig. 11),

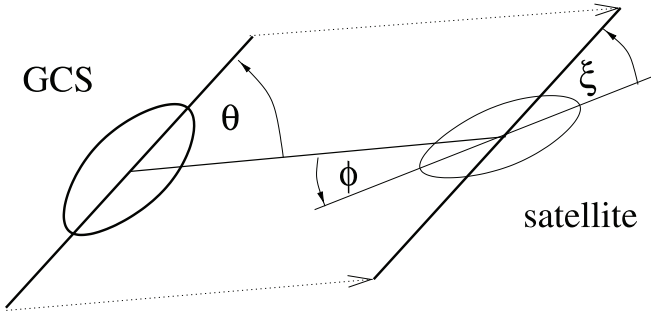


FIG. 11.—Three angles θ , ϕ , and ξ , which are used for halo alignment, radial alignment, and direct alignment, respectively (cf. Paper I).

and the projected orientations are referred to as position angles (P.A.s). It is not straightforward to derive galaxy properties, such as luminosity and color, from the dark matter distribution. In particular, if the satellite halo hosts a late-type galaxy, it is not obvious how to accurately determine the orientation of the disk (but see, e.g., Kang et al. [2007] and Agustsson & Brainerd [2007] for attempts). On the other side, if one focuses on early-type galaxies, the orientation of the central dark matter distribution is very likely correlated with the orientation of the stellar component (see the evidence from gravitational lensing, e.g., Kochanek 2002). The lower particle limit for the satellites results in a lower mass of $10^{11} h^{-1} M_\odot$ within $25 h^{-1}$ kpc. Assuming a dynamical mass-to-light ratio of a few (Cappellari et al. 2006) within this radius yields a stellar component that roughly resembles L_* galaxies. Therefore, our findings in the current paper may be best compared with results based on bright early-type satellite galaxies. However, as we have pointed out in Paper I, our observational results were only marginally dependent on the luminosity/mass of satellite galaxies. Therefore, a comparison with observations based on somewhat fainter satellites is viable as well.

5.1. Halo Alignment

Figure 12 shows the results obtained for the angle θ between the orientation of the GCS and the line connecting the GCS with the satellite. The short horizontal line on the left indicates the result for the innermost bin if only the satellites within $1r_{\text{vir}}$ are projected. The sample shows $\langle \theta \rangle < 45^\circ$ for the entire distance range. The error bars give the 95% bootstrap confidence intervals for the mean angles within each bin. The short horizontal line on the left indicates the signal for the innermost bin if only the satellites within three-dimensional distances $\leq 1r_{\text{vir}}$ are projected. The corresponding three-dimensional results are shown in Fig. 4.

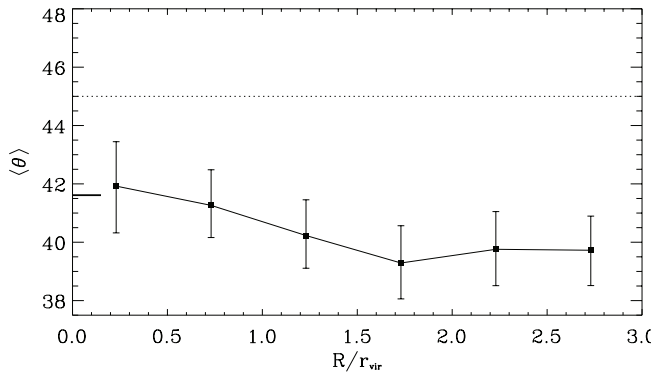


FIG. 12.—Mean angle, θ , between the P.A. of the GCS and the line connecting the GCS and a satellite, as a function of projected distance R/r_{vir} , with equidistant bins of $0.5r_{\text{vir}}$. The error bars give the 95% bootstrap confidence intervals for the mean angles within each bin. The short horizontal line on the left indicates the signal for the innermost bin if only the satellites within three-dimensional distances $\leq 1r_{\text{vir}}$ are projected. The corresponding three-dimensional results are shown in Fig. 4.

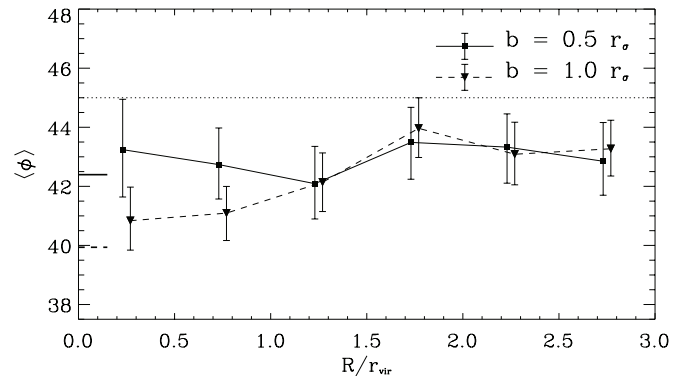


FIG. 13.—Same as Fig. 12, but for the angle ϕ . The radial dependence of the $b = 1r_\sigma$ sample is displayed as well. The corresponding three-dimensional results are shown in Fig. 5.

ervals for the mean angles within each bin. The alignment strength within r_{vir} is $\sim 42^\circ$, in good agreement with the findings of Brainerd (2005) and Yang et al. (2006). In Paper I we found a mean value $\theta \approx 41^\circ$ within $0.5r_{\text{vir}}$ that is very close to the values we obtain for the innermost bin, in particular if only the satellites within $1r_{\text{vir}}$ (short horizontal line on the left) are projected. As also shown by Agustsson & Brainerd (2006b), the alignment signal extends beyond the virial radius. The strongest amplitude is found outside the virial radius at $\sim 1.7r_{\text{vir}}$. Currently, there are no available observations covering the same distance range. The analysis in Paper I, for instance, is based on galaxies within the virial radius, whereas we use all galaxies with projected distances $\lesssim 3r_{\text{vir}}$. According to our findings, a search for alignment of satellite distribution in group environments for distances larger than r_{vir} may be a promising proposition.

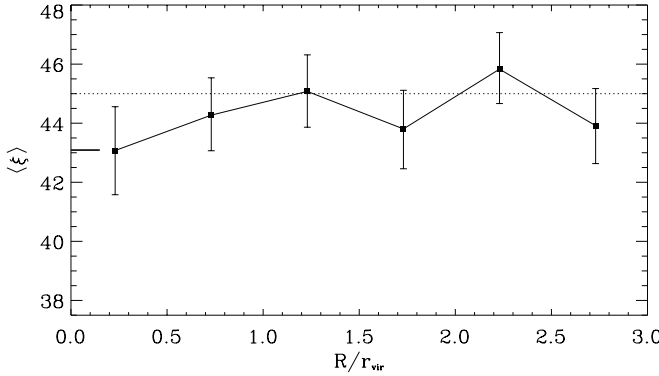
5.2. Radial Alignment

Figure 13 displays the mean angle ϕ between the P.A. of the satellite and the line connecting the satellite with its GCS. For all groupcentric distances, there is a clear and significant signal that the major axes of the satellites point toward the GCS (i.e., $\langle \phi \rangle < 45^\circ$). The projection of only those satellites within $1r_{\text{vir}}$ increases the central signal by about 1° (differences between the innermost data points and the short horizontal lines). The mean angle for the $0.5r_\sigma$ sample within the innermost bin is $\sim 43^\circ$, and according to Paper I, the mean value for the red SDSS satellites within $0.5r_{\text{vir}}$ is very close to this value. However, the observations suggest a significant alignment for red galaxies only out to $0.7r_{\text{vir}}$, whereas the N -body data indicate that radial alignment extends beyond $3r_{\text{vir}}$. The discrepancy may be caused by the observational confinement to galaxies within the virial radius.

5.3. Direct Alignment

Figure 14 displays the results for the direct alignment, based on the angle ξ between the orientations of GCSs and satellites. The alignment signal is significant at a $\gtrsim 95\%$ confidence level for distances $\lesssim 0.5r_{\text{vir}}$. In Paper I we obtained $\xi \approx 44^\circ$ for red satellites within $0.5r_{\text{vir}}$, which indicates a somewhat weaker alignment than we find here. Since the three-dimensional analysis shows no increase of $\langle |a_{\text{GCS}} \cdot r| \rangle$ at small scales (Fig. 4), the central enhancement displayed here has to be interpreted as a result of projection effects.

In summary, for all three types of alignments we find good agreement between the numerical data presented here and the observational results from Paper I. In particular, the relative

FIG. 14.—Same as Fig. 12, but for the angle ξ .

strength among the different alignments is well reproduced in the numerical analysis. Due to limited resolution, the range below $1r_{\text{vir}}$ is only sparsely sampled; thus no detailed information about the radial dependence of the alignment signal on small scales can be derived. However, the signal for θ increases with distance, which is only marginally implied by the SDSS results presented in Paper I. Also for ϕ , the dependence on the distance disagrees between simulations and observations. It is currently unclear whether this is due to shortcomings on the numerical or observational side.

6. SUMMARY

Based on a sample of 515 groups with masses ranging from 10^{13} to $5 \times 10^{14} h^{-1} M_{\odot}$, we have investigated the halo alignment, $\langle |\mathbf{a}_{\text{GCS}} \cdot \mathbf{r}| \rangle$, the radial alignment, $\langle |\mathbf{a}_{\text{SAT}} \cdot \mathbf{r}| \rangle$, and the direct alignment, $\langle |\mathbf{a}_{\text{GCS}} \cdot \mathbf{a}_{\text{SAT}}| \rangle$, between the central region of each group (the GCS) and its satellite halos out to a distance of $6r_{\text{vir}}$. Here \mathbf{a}_{GCS} , \mathbf{a}_{SAT} , and \mathbf{r} denote the unit vectors associated with the orientation of the GCS, the satellites, and the line connecting them, respectively. In addition, we have employed the directions of the satellite velocities \mathbf{v} to probe the alignments $\langle |\mathbf{v} \cdot \mathbf{r}| \rangle$, $\langle |\mathbf{a}_{\text{GCS}} \cdot \mathbf{v}| \rangle$, and $\langle |\mathbf{a}_{\text{SAT}} \cdot \mathbf{v}| \rangle$, referred to as radial velocity, halo velocity, and autovelocity alignments, respectively. Our main results are the following:

1. Halo, radial, and direct alignment differ in strength. The halo alignment is strongest, followed by the radial alignment. By far the weakest and least significant signal comes from the direct alignment. This sequence is found in the three-dimensional analysis, as well as in the projected data, and agrees well with our recent analysis of galaxy alignments in the SDSS (cf. Paper I).

2. The signal for the halo alignment, $\langle |\mathbf{a}_{\text{GCS}} \cdot \mathbf{r}| \rangle$, reaches far beyond the virial radii of the groups ($>6r_{\text{vir}}$), which we interpret as evidence for large-scale filamentary structure.

3. The signal for the radial alignment, $\langle |\mathbf{a}_{\text{SAT}} \cdot \mathbf{r}| \rangle$, is largest on small scales. After a rapid decline with distance it flattens, such that a relatively small $\langle |\mathbf{a}_{\text{SAT}} \cdot \mathbf{r}| \rangle \approx 0.52$ but significant deviation from isotropy is detected out to $\sim 6r_{\text{vir}}$. Whereas the small-scale signal more likely derives from the group's tidal field, the weak but significant signal on large scales suggests that satellites tend to be oriented along the filaments in which they reside.

4. The three-dimensional signal for the direct alignment, $\langle |\mathbf{a}_{\text{GCS}} \cdot \mathbf{a}_{\text{SAT}}| \rangle$, shows a weak trend for parallel orientations on scales $\lesssim 2r_{\text{vir}}$. The projected data indicate an increasing signal for distances $\lesssim 0.5r_{\text{vir}}$, which is likely caused by projection effects.

5. All kinetic alignment signals are highly significant at small scales. The signal for $\langle |\mathbf{v} \cdot \mathbf{r}| \rangle$ is basically constant within $2.0r_{\text{vir}}$,

beyond which it rapidly drops. In the subset of outward-moving satellites, we find a tendency for tangential motions that can be attributed to the satellites that were accreted earlier and are currently passing their peri- or apocenters. The signal for $\langle |\mathbf{a}_{\text{GCS}} \cdot \mathbf{v}| \rangle$ is maximal at the center, drops rapidly with distance, and disappears at $1r_{\text{vir}}$. Finally, $\langle |\mathbf{a}_{\text{SAT}} \cdot \mathbf{v}| \rangle$ shows a slight dip at the center, reaches a maximum at $0.7r_{\text{vir}}$, and becomes consistent with isotropy at $1.5r_{\text{vir}}$. All these features support the interpretations advocated for the spatial alignments.

The simulation analyzed here clearly demonstrates that tidal forces cause a variety of alignments among neighboring non-linear structures. On large scales, the tidal forces are responsible for creating a filamentary network, which gives rise to a halo alignment out to at least $6r_{\text{vir}}$. The same tidal forces also cause an alignment between filaments and (sub)structures within the filaments (cf. Altay et al. 2006; Hahn et al. 2007), which in turn results in a large-scale radial alignment with the virialized structures at the nodes of the cosmic web. Within these virialized structures, tidal forces are responsible for a radial alignment of its substructures, similar to the tidal locking mechanism that affects the Earth-Moon system. This is further supported by the fact that the autovelocity alignment $\langle |\mathbf{a}_{\text{SAT}} \cdot \mathbf{v}| \rangle$ reveals a dip on small scales, indicating that at pericentric passage satellites tend to be oriented perpendicular to the direction of their motion (cf. Kuhlen et al. 2007). This behavior also explains why the direct spatial alignment, $\langle |\mathbf{a}_{\text{GCS}} \cdot \mathbf{a}_{\text{SAT}}| \rangle$, is so weak. A possible direct alignment originating from the coevolution of group and satellites, as proposed by Lee et al. (2005), is quickly erased as the satellites orbit in the potential well of the group. For future work, it will be instructive to trace the orbits of individual satellites and consider more closely how their shapes and orientations evolve with time.

The infall regions around virialized dark matter halos cause a radial velocity alignment out to $\sim 2r_{\text{vir}}$ and an enhancement of inward-moving (sub)structures. At around the same scale, the (sub)structures with a net outward movement have a tendency to move tangentially. This most likely reflects the apocentric passage of substructures that have previously fallen through the virialized halo. Within a virialized region, the orientation of orbits is naturally aligned with that of its GCS. Since (sub)structures reveal at most a weak velocity bias with respect to dark matter particles (e.g., Faltenbacher & Diemand 2006), this causes a strong halo velocity alignment on scales $\lesssim r_{\text{vir}}$. The halo velocity alignment is also strong on large scales ($\gtrsim 3r_{\text{vir}}$), which reflects the Hubble flow combined with the filamentary, nonisotropic distribution of (sub)structures on these scales.

A one-to-one comparison between the N -body results discussed here and the observations presented in Paper I is not straightforward. Although we have employed the same mass range for the groups in both studies, the resolution of the current simulation allows us to resolve only satellites that are expected to host $\gtrsim L_*$ galaxies. These are bright compared to our SDSS sample, for which a lower magnitude limit of $0.1 M_r - 5 \log h \leq -19$ has been adopted. Nevertheless, the qualitative agreement between the relative strengths of the different types of spatial alignment is promising. Supplementary to the observational results of Paper I, we find a strong halo alignment and a somewhat weaker radial alignment out to at least $6r_{\text{vir}}$, which we will investigate further.

Finally, the weak but significant detection of radial alignment out to $6r_{\text{vir}}$ may contaminate the cosmic shear measurements on these scales. This correlation has to be considered, either by simply removing or downweighting pairs of galaxies within this distance range (King & Schneider 2002; Heymans & Heavens

2003). This may be particularly important for applications of weak gravitational lensing for the purposes of precision cosmology.

We are grateful to the anonymous referee, who helped us to significantly improve the original version of the draft. This work has is supported by NSFC (10533030, 10643005, 10643006, and

973 Program 2007 CB815402) and the Knowledge Innovation Program of the Chinese Academy of Sciences, grant KJCX2-YW-T05. The CAS Research Fellowship for International Young Researchers (A. F.), the local support of the Chinese Academy of Sciences (H. J. M. and S. M.), and the Alexander von Humboldt Foundation (S. M.) are gratefully acknowledged. H. J. M. would like to acknowledge the support of NSF ATP-0607535, NASA AISR-126270, and NSF IIS-0611948.

REFERENCES

- Adelman-McCarthy, J. K., et al. 2006, *ApJS*, 162, 38
 Agustsson, I., & Brainerd, T. G. 2006a, *ApJ*, 644, L25
 ———. 2006b, *ApJ*, 650, 550
 ———. 2007, *ApJ*, submitted (arXiv:0704.3441v1)
 Allgood, B., Flores, R. A., Primack, J. R., Kravtsov, A. V., Wechsler, R. H., Faltenbacher, A., & Bullock, J. S. 2006, *MNRAS*, 367, 1781
 Altay, G., Colberg, J. M., & Croft, R. A. C. 2006, *MNRAS*, 370, 1422
 Aragón-Calvo, M. A., van de Weygaert, R., Jones, B. J. T., & van der Hulst, J. M. 2007, *ApJ*, 655, L5
 Azzaro, M., Patiri, S. G., Prada, F., & Zentner, A. R. 2007, *MNRAS*, 376, L43
 Bailin, J., Power, C., Norberg, P., Zaritsky, D., & Gibson, B. K. 2007, *MNRAS*, submitted (arXiv:0706.1350)
 Bailin, J., & Steinmetz, M. 2005, *ApJ*, 627, 647
 Basilakos, S., Plionis, M., Yepes, G., Gottlöber, S., & Turchaninov, V. 2006, *MNRAS*, 365, 539
 Binggeli, B. 1982, *A&A*, 107, 338
 Binney, J., & Tremaine, S. 1987, *Galactic Dynamics* (Princeton: Princeton Univ. Press)
 Brainerd, T. G. 2005, *ApJ*, 628, L101
 Bullock, J. S. 2002, in *The Shapes of Galaxies and Their Dark Matter Halos*, ed. P. Natarajan (Singapore: World Scientific), 109
 Cappellari, M., et al. 2006, *MNRAS*, 366, 1126
 Carter, D., & Metcalfe, N. 1980, *MNRAS*, 191, 325
 Catelan, P., Kamionkowski, M., & Blandford, R. D. 2001, *MNRAS*, 320, L7
 Chambers, S. W., Melott, A. L., & Miller, C. J. 2002, *ApJ*, 565, 849
 Ciotti, L., & Dutta, S. N. 1994, *MNRAS*, 270, 390
 Colín, P., Klypin, A. A., & Kravtsov, A. V. 2000, *ApJ*, 539, 561
 Colless, M., et al. 2001, *MNRAS*, 328, 1039
 Crittenden, R. G., Natarajan, P., Pen, U.-L., & Theuns, T. 2001, *ApJ*, 559, 552
 Croft, R. A. C., & Metzler, C. A. 2000, *ApJ*, 545, 561
 Davis, M., Efstathiou, G., Frenk, C. S., & White, S. D. M. 1985, *ApJ*, 292, 371
 Dekel, A. 1985, *ApJ*, 298, 461
 Diemand, J., Moore, B., & Stadel, J. 2004, *MNRAS*, 352, 535
 Faltenbacher, A., Allgood, B., Gottlöber, S., Yepes, G., & Hoffman, Y. 2005, *MNRAS*, 362, 1099
 Faltenbacher, A., & Diemand, J. 2006, *MNRAS*, 369, 1698
 Faltenbacher, A., Gottlöber, S., Kerscher, M., & Müller, V. 2002, *A&A*, 395, 1
 Faltenbacher, A., Li, C., Mao, S., van den Bosch, F. C., Yang, X., Jing, Y. P., Pasquali, A., & Mo, H. J. 2007, *ApJ*, 662, L71 (Paper I)
 Faltenbacher, A., & Mathews, W. G. 2007, *MNRAS*, 375, 313
 Ghigna, S., Moore, B., Governato, F., Lake, G., Quinn, T., & Stadel, J. 1998, *MNRAS*, 300, 146
 Hahn, O., Carollo, C. M., Porciani, C., & Dekel, A. 2007, *MNRAS*, 381, 41
 Hawley, D. L., & Peebles, P. J. E. 1975, *AJ*, 80, 477
 Heavens, A., Refregier, A., & Heymans, C. 2000, *MNRAS*, 319, 649
 Heymans, C., & Heavens, A. 2003, *MNRAS*, 339, 711
 Holmberg, E. 1969, *Ark. Astron.*, 5, 305
 Hopkins, P. F., Bahcall, N. A., & Bode, P. 2005, *ApJ*, 618, 1
 Jing, Y. P. 2002, *MNRAS*, 335, L89
 Jing, Y. P., & Suto, Y. 2002, *ApJ*, 574, 538
 Kang, X., Mao, S., Gao, L., & Jing, Y. P. 2005, *A&A*, 437, 383
 Kang, X., van den Bosch, F. C., Yang, X., Mao, S., Mo, H. J., Li, C., & Jing, Y. P. 2007, *MNRAS*, 378, 1531
 Kasun, S. F., & Evrard, A. E. 2005, *ApJ*, 629, 781
 King, L., & Schneider, P. 2002, *A&A*, 396, 411
 Knebe, A., Gill, S. P. D., Gibson, B. K., Lewis, G. F., Ibata, R. A., & Dopita, M. A. 2004, *ApJ*, 603, 7
 Koch, A., & Grebel, E. K. 2006, *AJ*, 131, 1405
 Kochanek, C. S. 2002, in *The Shapes of Galaxies and Their Dark Matter Halos*, ed. P. Natarajan (Singapore: World Scientific), 62
 Kroupa, P., Theis, C., & Boily, C. M. 2005, *A&A*, 431, 517
 Kuhlen, M., Diemand, J., & Madau, P. 2007, *ApJ*, 671, 1135
 Lee, J., Kang, X., & Jing, Y. P. 2005, *ApJ*, 629, L5
 Libeskind, N. I., Cole, S., Frenk, C. S., Okamoto, T., & Jenkins, A. 2007, *MNRAS*, 374, 16
 Libeskind, N. I., Frenk, C. S., Cole, S., Helly, J. C., Jenkins, A., Navarro, J. F., & Power, C. 2005, *MNRAS*, 363, 146
 Lynden-Bell, D. 1982, *Observatory*, 102, 202
 Macciò, A. V., Moore, B., Stadel, J., & Diemand, J. 2006, *MNRAS*, 366, 1529
 MacGillivray, H. T., Dodd, R. J., McNally, B. V., & Corwin, H. G., Jr. 1982, *MNRAS*, 198, 605
 Majewski, S. R. 1994, *ApJ*, 431, L17
 Onorai, L. I., & Thomas, P. A. 2000, *MNRAS*, 319, 614
 Pen, U.-L., Lee, J., & Seljak, U. 2000, *ApJ*, 543, L107
 Pereira, M. J., Bryan, G. L., & Gill, S. P. D. 2008, *ApJ*, 672, 825
 Pereira, M. J., & Kuhn, J. R. 2005, *ApJ*, 627, L21
 Plionis, M. 1994, *ApJS*, 95, 401
 Plionis, M., & Basilakos, S. 2002, *MNRAS*, 329, L47
 Plionis, M., Benoist, C., Maurogordato, S., Ferrari, C., & Basilakos, S. 2003, *ApJ*, 594, 144
 Porciani, C., Dekel, A., & Hoffman, Y. 2002, *MNRAS*, 332, 339
 Rhee, G. F. R. N., & Latour, H. J. 1991, *A&A*, 243, 38
 Sharp, N. A., Lin, D. N. C., & White, S. D. M. 1979, *MNRAS*, 187, 287
 Stadel, J. G. 2001, Ph. D. thesis, Univ. Washington
 Statler, T. S. 1987, *ApJ*, 321, 113
 Struble, M. F. 1990, *AJ*, 99, 743
 Tormen, G. 1997, *MNRAS*, 290, 411
 Ulmer, M. P., McMillan, S. L. W., & Kowalski, M. P. 1989, *ApJ*, 338, 711
 van den Bosch, F. C., Lewis, G. F., Lake, G., & Stadel, J. 1999, *ApJ*, 515, 50
 Wang, H. Y., Jing, Y. P., Mao, S., & Kang, X. 2005, *MNRAS*, 364, 424
 West, M. J. 1989, *ApJ*, 344, 535
 Yang, X., Mo, H. J., van den Bosch, F. C., & Jing, Y. P. 2005, *MNRAS*, 356, 1293
 Yang, X., van den Bosch, F. C., Mo, H. J., Mao, S., Kang, X., Weinmann, S. M., Guo, Y., & Jing, Y. P. 2006, *MNRAS*, 369, 1293
 York, D. G., et al. 2000, *AJ*, 120, 1579
 Zaritsky, D., Smith, R., Frenk, C. S., & White, S. D. M. 1997, *ApJ*, 478, L53
 Zentner, A. R., Kravtsov, A. V., Gnedin, O. Y., & Klypin, A. A. 2005, *ApJ*, 629, 219